Solar Energy 198 (2020) 586–595

Contents lists available at ScienceDirect

Solar Energy

journal homepage: www.elsevier.com/locate/solener

Study of $(Ag_xCu_{1-x})_2ZnSn(S,Se)_4$ monograins synthesized by molten salt method for solar cell applications

S. Oueslati[a,b,*], M. Kauk-Kuusik[a], C. Neubauer[b], V. Mikli[a], D. Meissner[a,b], G. Brammertz[c], B. Vermang[c], J. Krustok[a,d], M. Grossberg[a]

[a] Department of Materials and Environmental Technology, Tallinn University of Technology, Ehitajate tee 5, 19086 Tallinn, Estonia
[b] Crystalsol OÜ, Akadeemia tee 15a, 12618 Tallinn, Estonia
[c] Imec division IMOMEC (Partner in Solliance and Energyville), Thorpark 8320, 3600 Genk, Belgium
[d] Divison of Physics, Tallinn University of Technology, Ehitajate tee 5, 19086 Tallinn, Estonia

ARTICLE INFO

Keywords:
Copper zinc tin sulfur selenide
Kesterite
Cations substituation
Monograins
Photoluminescence
Electron beam induced current

ABSTRACT

The open circuit voltage (V_{OC}) deficit of $Cu_2ZnSn(S,Se)_4$ (CZTSSe) kesterite solar cells is higher than that of the closely related $Cu(InGa)Se_2$ solar cells. One of the most promising strategies to overcome the large V_{OC} deficit of kesterite solar cells is by reducing the recombination losses through appropriate cation substitution. In fact, replacing totally or partially Zn or Cu by an element with larger covalent radius one can significantly reduce the concentration of I–II antisite defects in the bulk. In this study, an investigation of the impact of partial substitution of Cu by Ag in CZTSSe solid solution monograins is presented. A detailed photoluminescence study is conducted on Ag-incorporated CZTSSe monograins and a radiative recombination model is proposed. The composition and structural quality of the monograins in dependence of the added Ag amount are characterized using Energy Dispersive X-ray Spectroscopy and X-Ray Diffraction method, respectively. The Ag-incorporated CZTSSe monograin solar cells are characterized by temperature dependent current-voltage and electron beam induced current methods. It was found, that low Ag contents ($x \leq 0.02$) in CZTSSe lead to higher solar cell device efficiencies.

1. Introduction

The p-type semiconductor $Cu_2ZnSn(S,Se)_4$ (CZTSSe) has been the subject of intensive studies over the last decade as an attractive, non-toxic absorber for sustainable solar cells. CZTSSe is a challenging semiconductor compound. Although a promising efficiency of 12.6% of kesterite-based solar cells was reached in 2013 (Wang et al., 2014), further advancements have been limited mainly by the non-optimized absorber properties and the device structure (Siebentritt, 2013). Among all the efficiency limitations, the low open circuit voltage (V_{OC}) of the solar cells compared to their theoretical maximum given by the Shockley-Queisser limit (Shockley and Queisser, 1961) seems to be the most critical issue to solved. The high density of bulk defect states and the atomic disorder are accused to cause band tailing leading to the large V_{OC} deficit in kesterite solar cells (Oueslati et al., 2019; Barkhouse et al., 2012). The Cu_{Zn} antisite formation results from the low enthalpy of formation of the associated defect due to the similarity of the covalent radiuses of Cu^+ (0.74 Å) and Zn^{2+} (0.74 Å) cations (Li et al., 2018) leading to high concentration of bulk defects, pinning of the Fermi level in the middle of the bandgap and limiting the V_{OC} of the device (Chen et al., 2013). One of the most promising strategies to overcome the large V_{OC} deficit is by reducing recombination losses related to Cu–Zn disorder in the absorber through appropriate cation substitution. In fact, replacing Zn or Cu completely or partially by an element with a larger covalent radius increases the enthalpy penalty for the I–II site exchange, which should significantly reduce the concentration of bulk defects (Gershon et al., 2016). Silver (Ag^+) with a relatively large covalent radius of about 1.14 Å (Li et al., 2018) is a good candidate to replace the Cu^+. Both elements belong to the same chemical group and partial substitution of Cu by Ag in the CZTSSe system will likely suppress the cation disordering and the associated band tailing. Furthermore, Ag-incorporated $Cu_2ZnSn(S,Se)_4$ offers a way for widening the bandgap making this compound an important candidate for tandem solar cell applications (Jing et al., 2015). The influence of Ag incorporation on the CZTSSe thin film solar cell device performance has already been studied by several research groups (Gershon et al., 2016; Guchhait et al., 2016; Qi et al., 2017). Gershon et al. reported that the extent of band tailing in the $Cu_2ZnSnSe_4$ (CZTSe) semiconductor is

* Corresponding author at: Tallinn University of Technology, Ehitajate tee 5, Tallinn 19086, Estonia.
E-mail address: souhaib.oueslati@taltech.ee (S. Oueslati).

https://doi.org/10.1016/j.solener.2020.02.002
Received 18 November 2019; Received in revised form 15 January 2020; Accepted 1 February 2020

decreasing with increasing the content of Ag based on the comparison of the optical bandgap extrapolated from transmission data and the position of the room-temperature photoluminescence peak (Gershon et al., 2016). Guchhait et al. reported an increase of the V_{OC} and device efficiency resulting from the incorporation of Ag in Cu_2ZnSnS_4 (CZTS) which is found to improve the grain size, enhance the depletion width of the p-n junction and reduce the concentration of antisite defect states (Guchhait et al., 2016). Qi et al. showed that the power conversion efficiency of the solar cells based on the Ag-incorporated CZTSSe absorbers was successfully improved from 7.39 to 10.36% by reducing the formation of Cu_{Zn} antisite defects as evaluated by the deep-level transient spectroscopy technique (Qi et al., 2017). There is no clear correlation between the measured Ag concentration in the absorber layer and the claimed improvement of the solar cell parameters among the cited studies. In fact, only low Ag content (lower than 10%) is reported to be beneficial for solar cell performance whereas higher amounts lead to lower performance as found in (Gershon et al., 2016; Qi et al., 2017). Few reports focused on the substitution impact on the fundamental properties of the material. A systematic research on the crystallographic and optical properties of both types $(Ag,Cu)_2ZnSnS_4$ (ACZTS) and $(Ag,Cu)_2ZnSnSe_4$ (ACZTSe) solid solutions with a varied ratio of [Ag]/([Ag] + [Cu]) was performed by Gong et al. confirming the tetragonal kesterite-type structure in both cases (Gong et al., 2015). However, very little information is known about the electronic properties of $(Ag_xCu_{1-x})_2ZnSn(S,Se)_4$ (ACZTSSe) in the form of solid solution monograins for photovoltaic applications. Inspired by the above mentioned encouraging experimental results obtained using thin film absorber layer, the present study aims to reveal the effect of partial substitution of Cu with different amounts of Ag in the kesterite monograins on its electronic and optoelectronic properties. A detailed photoluminescence (PL) study is conducted on ACZTSSe monograins and a radiative recombination model is proposed. The corresponding ACZTSSe monograin solar cells were studied by temperature dependent current-voltage (IVT), external quantum efficiency (EQE) and electron beam induced current (EBIC) methods.

2. Experiment description

2.1. Synthesis of ACZTSSe monograins

The ACZTSSe monograins were synthesized in molten flux potassium iodide (KI) at 740 °C (above the melting temperature of the flux) for 88 h from elemental 5 N purity precursors: Cu, Ag, Zn, Sn, Se and S. The mixture of the precursors and flux were inserted into quartz ampoules. The Ag is added as elemental precursor to the precursors mixture in various concentrations and the ratio [Ag]/([Ag] + [Cu]) is presented as x throughout the manuscript referring to the input amounts introduced to the system. The Ag-incorporated kesterite solar cells usually adopt low Ag content (lower than 10%). The contents investigated here are × = 0, 0.01, 0.02, 0.03, 0.04, 0.05 and 0.08. The Ag-free sample (x = 0) is considered as a reference material. After the synthesis of the monograins, the flux (KI) was removed by washing with deionized water at room temperature, after which the monograins are dried and sieved to narrow fractions (Additional Material Fig. A1a). A heat treatment step at 740 °C for 35 min is needed to heal the monograin's surface.

2.2. Solar cell devices fabrication

To form a p-n junction on each monograin, the heat-treated monograins were covered by a thin cadmium sulphide (CdS) layer using the chemical bath deposition method. By partially embedding the monograins with desired size (50 to 60 μm) in a thin layer of polymer, so-called monograin layer (MGL) is prepared (Additional Material Fig. A1b). Solar cell devices where the monograins are connected in parallel are completed in a standard process using i-ZnO/ZnO:Al as a front contact and graphite as a back contact. A more detailed description of monograin synthesis and the device preparation can be found elsewhere (Kauk-Kuusik et al., 2018; Neubauer et al., 2018).

2.3. Characterization and analysis

The composition and structural quality of the monograins were characterized using Energy Dispersive X-ray Spectroscopy (EDX) and X-Ray Diffraction (XRD) methods, respectively. The EDX study was performed on a Zeiss MERLIN scanning electron microscope operated with an accelerating voltage of 20 kV using a Röntec EDX XFlash 3001 detector. The cross-section electron beam induced current (EBIC) investigation was conducted with the same instrument. The crystal structure of the studied ACZTSSe monograins was determined by XRD using a Rigaku Ultima IV diffractometer with monochromatic Cu Kα1 radiation (λ = 1.5406 Å) at 40 kV and 40 mA operating with the silicon strip detector D/teX Ultra. The phase analysis and lattice parameters calculations were made using software on the Rigaku's system PDXL2. Time resolved photoluminescence (TRPL) measurements were acquired with a Hamamatsu C12132 near infrared compact fluorescence lifetime measurement system, in which the monograins were illuminated with a 15 kHz, 1.5 ns pulsed 532 nm laser with 1.38 mW average laser power. For photoluminescence (PL) measurements, the samples were mounted in a closed-cycle He cryostat enabling variation of temperature between 10 and 300 K. The 442 nm He-Cd laser line was used as an excitation source and its intensity was attenuated with a range of neutral density filters. An InGaAs detector from Hamamatsu was used to detect the PL signal. The current-voltage (I-V) measurements at room temperature were performed under AM1.5 illumination condition using a Newport Oriel solar simulator system (class AAA). For the temperature-dependent current-voltage measurements, solar cells were mounted in a closed-cycle He cryostat. The I-V(T) curves were measured with a Keithley 2401 Source Meter under 100 mW/cm^2 illumination using calibrated intensity from a halogen lamp. The external quantum efficiency (EQE) measurements were carried out by means of a Newport Oriel 300 W Xenon lamp with a Cornerstone 260 monochromator at room temperature. The EQE measurements were done under chopped light in the wavelength range between 350 nm and 1100 nm. For impedance measurements at room temperature, a Wayne Kerr 6500B impedance analyser was used. The measurements were carried out in the dark with AC voltage amplitude of 10 mV and DC bias of 0 V.

3. Results

3.1. Structural characterization

3.1.1. Materials composition

The different amounts of Ag introduced as input to substitute the Cu and the actual Ag amounts measured with EDX in the investigated samples are summarized in Fig. 1a. For monograins with × = 0.01 and 0.02, the EDX analysis shows that roughly all the introduced Ag was incorporated in the formed solid solution. However, for x > 0.03, the Ag concentration measured by EDX becomes considerably lower compared to the introduced amounts, but still increasing monotonously with increasing the introduced Ag amounts without reaching saturation. EDX analysis of the reclaimed KI flux after the synthesis suggests that the missing Ag amounts end up in the flux forming silver iodide (AgI). An equilibrium between the liquid and the solid phases during synthesis probably leads to the AgI formation. It is worth noting that the synthesized ACZTSSe samples were slightly (Cu and Ag)-poor with ([Cu] + [Ag]/([Zn] + [Sn]) < 1), Zn-rich ([Zn]/([Sn]) > 1) and S-rich ([S]/([S] + [Se]) = 0.6), as determined by EDX and presented in Table A1 in Additional Material. Although not all the Cu is substituted with the introduced amount of Ag in the cases of x > 0.03, the corresponding ([Cu] + [Ag])/([Zn] + [Sn]) ratio remained in the range of 0.9, indicating the ability of the formed compounds to readjust and

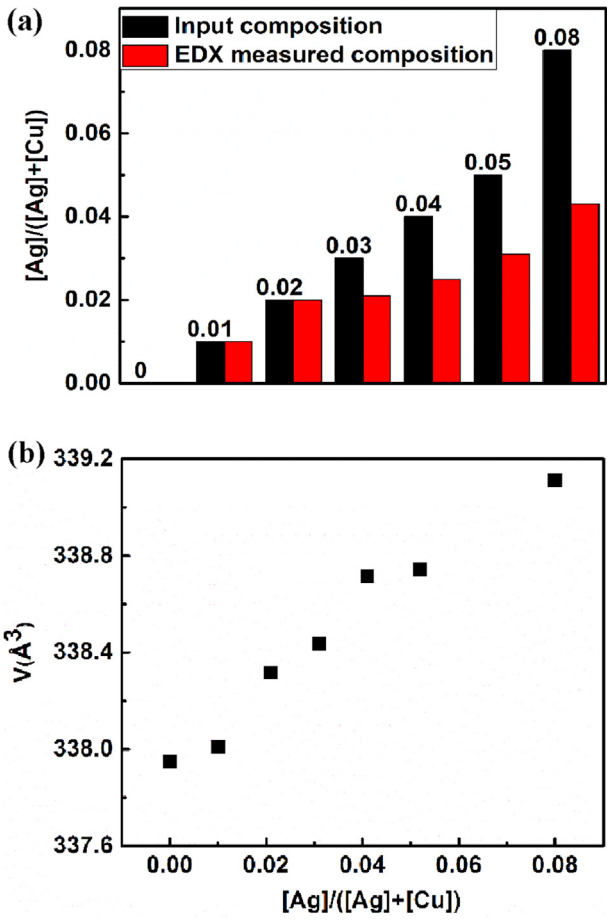

Fig. 1. (a) Amount of input x compared to the measured x in $(Ag_xCu_{1-x})_2ZnSn(S,Se)_4$ monograins using EDX, (b) Evolution of the tetragonal unit cell volume versus the input Ag contents x.

form a copper-poor/zinc-rich composition. The readjustment of the composition is accompanied by the formation of corresponding amounts of Zn or Sn-based secondary phases. The EDX line scan composition within the synthesized monograins shows uniform elemental distribution as shown in Additional Material Fig. A2.

3.1.2. XRD results

The powder X-ray diffraction investigations were carried out with all the studied samples and are presented in Additional Material Fig. A3a. The data show major peaks at 2θ = 27.9°, 46.4° and 55.1°, which can be indexed as 112, 220 and 312 planes, corresponding unambiguously to the kesterite structure (Nateprov et al., 2013). The most intensive 112 peak at 2θ = 27.97° of CZTSSe shifts slightly to lower angles with increasing Ag concentration as shown in Additional Material Fig. A3b. The shift of the 112 peak to lower angles implies an increase in lattice parameter values due to the replacement of relatively smaller atomic radius Cu^+ and/or Zn^{2+} with a larger atomic radius Ag^+; thereby increasing the unit cell volume. Fig. 1b confirms that the unit cell volume increases monotonously with increasing the Ag content. This could be explained by the larger bond valence parameters for Ag than for Cu leading to the observed bond distances (Ag—S bond is longer than Cu—S bond) (Yuan et al., 2015). Although no secondary phases weredetected, the presence of Zn(S,Se) and $Cu_2Sn(S,Se)_3$ phases cannot be excluded since their peaks overlap with those of CZTSSe and therefore cannot be distinguished by XRD (Dale et al., 2009).

3.1.3. Lifetime results

TRPL is a technique frequently used to estimate the minority carrier lifetime in the direct bandgap absorber layer of photovoltaic devices. Measuring the minority-carrier lifetime could help to understand the impact of changes of the material quality as a function of the amount of Ag. The samples are excited using an ultrafast laser pulse and the decay of the photoluminescence signals with time were acquired and are shown in Additional Material Fig. A4a. However, the determination of minority-carrier lifetime is not that straightforward. In fact, the TRPL signal could be a complex convolution of multiple physical factors such as bulk carrier lifetime, interface recombination velocity, electric field, doping density, photo-excited carrier density, and carrier mobility (Kanevce et al., 2013). To avoid the carrier drift due to the junction field, the TRPL measurements were carried out on monograins without CdS layer. The minority carrier lifetime, τ is determined from the decay time of the charge carrier recombination. In order to evaluate τ, the TRPL decay curves were fitted with a multiple exponential functions based on the following equation (Brammertz et al., 2013):

$$I_{PL}(t) = \sum_{i}^{n} C_i e^{-\frac{t}{\tau_i}} \quad (1)$$

in which $I_{PL}(t)$ represents the luminescence intensity at time t after the excitation pulse, C_i are coefficients and τ_i are different decay times. The fitting of the TRPL decay in ACZTSSe monograins has shown a good match with the experimentally measured decays using three different exponential components as shown in Additional Material Fig. A4b. The deconvoluted fitting parameters are summarized in Table 1. The first decay time τ_1 is very short and usually linked to the charge separation time in an electric field (even for monograins, there is usually a surface field due to interface defects) (Kanevce et al., 2013). The second decay time τ_2 can be ascribed to the charge carrier recombination time (Brammertz et al., 2013), whereas the longest decay τ_3 seems to be a trapping time in a defect level which delays the recombination. This interpretation is still under debate for kesterite materials (Li et al., 2019; Hages et al., 2017). Using percentage weighting of the amplitude of the three exponential components, we can provide clear understanding of which component dominates the decay dynamics as a function of Ag amount. An example of decay curve fittings of the reference powder is presented in Additional Material Fig. A4c.

It is clear that exclusion of the trapping time τ_3 is not detrimental for the evaluation of the injection minority carrier lifetime. The faster part of the decay τ_1 related to charge separation is dominating the decay curves. The slower recombination time $\tau_2$seems to be more relevant for the evaluation of the minority carrier lifetime in the ACZTSSe monograins and its dependence on the amount of introduced Ag as shown in Fig. 2. The lifetime (τ_2) of ACZTSSe monograins with × = 0.02 increased compared to Ag-free monograins CZTSSe. However, by further

Table 1
Decay parameters obtained by using fitting equation (1).

[Ag]/([Ag] + [Cu])	τ_1 (ns)	C_1 (%)	τ_2 (ns)	C_2 (%)	τ_3 (ns)	C_3 (%)
0	0.52 ± 0.02	72.51	3.40 ± 0.06	26.70	34.93 ± 1.95	0.79
0.02	0.79 ± 0.04	74.09	5.53 ± 0.23	20.83	109.52 ± 2.39	5.08
0.04	0.47 ± 0.02	72.90	2.59 ± 0.06	25.98	28.58 ± 1.42	1.11
0.05	0.39 ± 0.02	80.31	2.74 ± 0.07	18.78	39.12 ± 1.98	0.91
0.08	0.09 ± 0.002	96.55	0.58 ± 0.03	3.33	7.95 ± 0.70	0.12

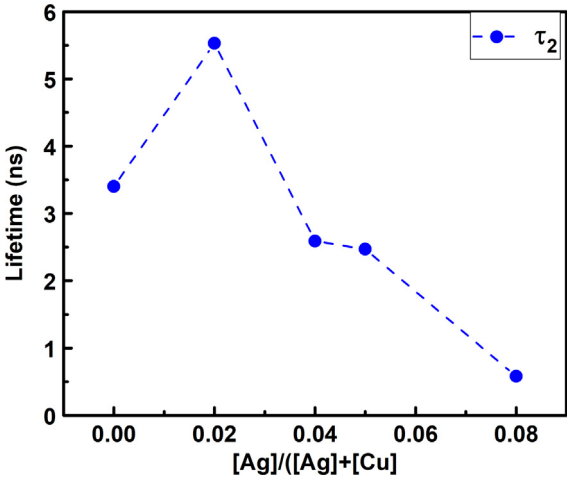

Fig. 2. The low injection minority carrier lifetime in the ACZTSSe monograins as a function of different amounts of Cu substituted by Ag.

increasing the amount of Ag, a pronounced decrease of lifetime is detected suggesting that higher concentrations of defects or non-radiative recombination centers were introduced to the material by substituting more Cu by Ag.

3.1.4. Photoluminescence results

Photoluminescence spectroscopy (PL) measurements offer an opportunity to study the electronic structure of semiconductors in general and in particular defect states within the bandgap. Studies of the temperature and excitation power dependent PL spectra offer an opportunity to explorethe recombination mechanisms within the kesterite monograins and to understand the effect of Ag incorporation to it. A detailed PL study was performed on samples (few heat-treated monograins embedded in a non-radiating polymer) with different Ag contents of × = 0, 0.02, 0.05 and 0.08. The PL spectra at 10 K of the studied samples have an asymmetric shape with much steeper decline on the high-energy side compared to the low-energy side as shown in Fig. 3. This kind of shape is quite common in chalcopyrite and kesterite materials (Grossberg et al., 2009; Krustok et al., 1999; Sulimov et al., 2019). From an exponential fit of the low-energy side of the PL spectra at T = 10 K an average depth of fluctuations (γ) can be estimated (Levanyuk and Osipov, 1981). The extracted γ values are 78.6 meV, 80.4, 101.8 meV and 98.1 meV for samples with × = 0, 0.2, 0.05 and 0.08 of Ag substitution, respectively. The γ values show a tendency to increase as the Ag content increases.

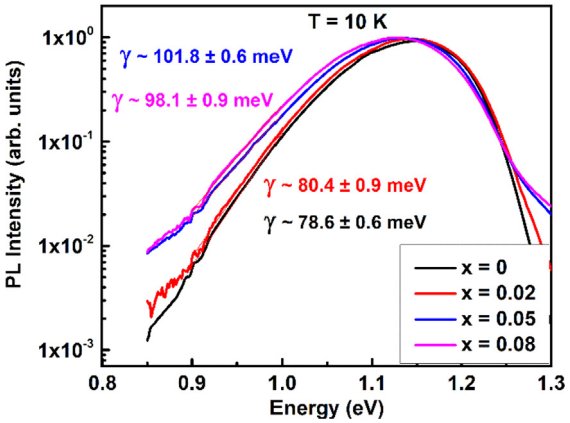

Fig. 3. PL spectra of the investigated powders at T = 10 K. γ values show the estimation of the average depth of the sum of potential and bandgap fluctuations.

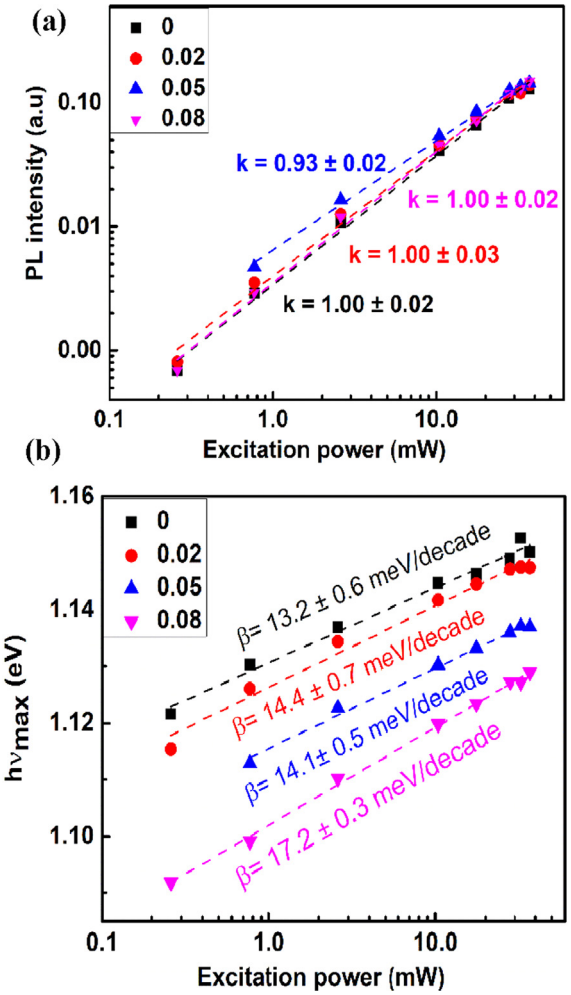

Fig. 4. Dependences of (a) the PL intensity and (b) the peak position, as a function of the excitation power at T = 10 K for ACZTSSe monograins with various Ag contents.

At a fixed temperature of T = 10 K, the excitation power i.e. carrier concentration dependence of the PL spectra was measured by changing the excitation power by almost three orders of magnitude. The excitation power dependence of PL intensity is generally a good indicator for identifying the nature of the radiative recombination processes. The dependence is described by a power law $I_{PL} \infty P_{ex}^{\ k}$ (k is the power coefficient estimated from a linear fit of the log–log plot of $I_{PL}(P_{ex})$). The empirical asymmetric double sigmoidal function (DSF) provides reasonable fitting of the PL spectra (Yakusheva et al., 2017):

$$I(h\nu) = A\left[1/\left(1 + exp\left(-\frac{h\nu - E_1}{W_1}\right)\right)\right] \times \left[1 - 1/\left(1 + exp\left(-\frac{h\nu - E_2}{W_2}\right)\right)\right] \quad (2)$$

where A, E_1, E_2, W_1 and W_2 are fitting parameters. The fitting results are shown in Fig. 4a and the extracted slope k is lower or equal to unity indicating that the radiative recombination involves localized defects with energy levels within the bandgap (Oueslati et al., 2015). The PL peak positions of the investigated samples as a function of the excitation power show significant blue-shifts, so called j-shift, as shown in Fig. 4b. The rate of the shift per decade of increasing laser power (β) grows from 13.2 meV/decade for Ag-free sample to 17.2 meV/decade for ACZTSSe sample with × = 0.08. Such a significant j-shift of the PL spectra along with its asymmetric shape at low temperature are characteristic features of materials with high concentration of charged defects (Sulimov et al., 2019).

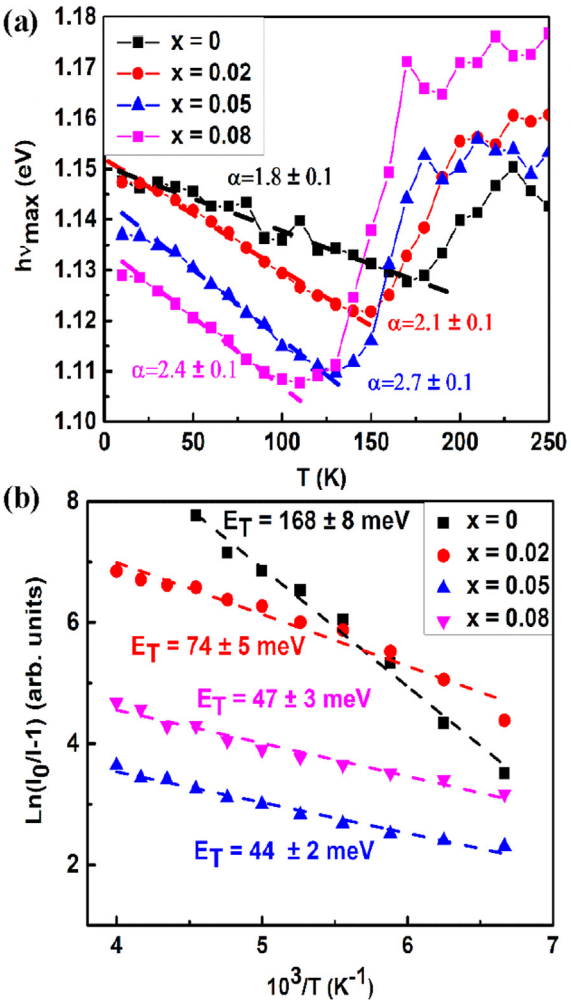

Fig. 5. (a) Temperature dependence of the PL peak position, (b) temperature dependence of the integrated intensities, dashed lines show the fitting results using Eq. (5).

In order to identify the nature of the radiative recombination mechanism associated with the studied samples the extraction of the activation energy of the transitions is mandatory. Temperature-dependent PL under fixed excitation power density of about 500 W/cm^2 was measured between 10 and 250 K. The temperature dependencies of the peak positions of the PL spectra $h\nu_{max}(T)$ of the studied powders are depicted in Fig. 5a. The $h\nu_{max}(T)$ shows a red-shift with increasing temperature up to a characteristic temperature (T_C) representing the minimum value of $h\nu_{max}(T)$. With further increase of the temperature, the $h\nu_{max}(T)$ shifts towards higher energies. The monotonic decrease of $h\nu_{max}(T)$ at low temperatures is more rapid than the bandgap shift with temperature and it can be expressed as (Krustok et al., 1999):

$$h\nu_{max}(T) = E_g^0 + \mu_n - \sqrt{2}\gamma - \varepsilon_1 \quad (3)$$

$$\text{with} \quad \varepsilon_1 = k_B T \ln\frac{N_v}{p + n\theta} \quad (4)$$

where E_g^0 is the energy gap without fluctuations, μ_n is the Fermi energy of the electrons, N_v is the effective density of states in the valence band, n and p are the concentrations of free electrons and holes, respectively, and θ is the ratio of electron and hole capture probabilities by the localized states.

The shift of $h\nu_{max}(T)$ can be simplified to a linear behaviour at temperatures below T_C as presented in Fig. 5a. Slope values α of about 1.8, 2.1, 2.7 and 2.4 corresponding to $\ln(N_v/(p + n\theta))$ deduced for powders with × = 0, 0.02, 0.05 and 0.08 respectively. The α values show a trend towards higher values with increasing amount of Ag. According to Eq. (4), higher α values correspond to lower carrier concentrations ($p + n\theta$) or to higher effective density of states in the valence band N_v. The shift of the PL peak positions $h\nu_{max}$ towards higher energies with increasing the excitation intensity observed in Fig. 4b is consistent with Eqs. (3) and (4), where the concentrations of free electrons and holes increase with higher excitation intensities.

The temperature dependences of the integrated PL intensities can be fitted according to the exponential law (Krustok et al., 2016):

$$I(T) = I_0[1 + A\exp(-E_T/k_B T)] \quad (5)$$

where $I(T)$ represents the integrated PL intensity at temperature T, I_0 is the integrated PL intensity when the temperature approaches T ~ 0 K, A is a fitting parameter, E_T is a thermal activation energy and k_B is the Boltzmann constant.

A linear fit of $Ln(I_0/I - 1)$ versus $1/T$ leads to a slope corresponding to E_T according to Eq. (5). The fitted lines are presented in Fig. 5b as dashed lines. A thermal activation energy of about 168 meV was extracted for the reference material CZTSSe, while lower activation energies of about 74 meV, 44 meV and 47 meV were extracted for materials with × = 0.02, 0.05 and 0.08, respectively. The kesterite materials are characterized by the presence of high concentrations of charged defects so that potential fluctuations start to affect the recombination processes and two radiative recombination pathways are likely dominating at low temperatures: (1) band-to-tail transition (BT) – the recombination of holes, localized in acceptor-like states of the valence band tail, with free electrons from the conduction band, and (2) the band-to-impurity transition (BI) – the recombination of free electrons with holes localized in acceptor states, which are deeper than the mean energy depth of potential fluctuations (Levanyuk and Osipov, 1981; Krustok et al., 1999). The significant j-shift of the PL spectra observed in Fig. 4b along with its asymmetric shape at low temperatures are characteristic features of BT or BI transitions in materials with high charged defects concentration (Grossberg et al., 2011). The E_T of the reference sample is higher than the estimated depth of the sum of potential and bandgap fluctuations indicating that the PL spectrum at low temperatures is related to BI transitions. The E_T of the Ag-substituted samples are lower than the estimated depth of the sum of potential and bandgap fluctuations, suggesting that the PL spectra at low temperatures originate from the BT transitions. Thus, the Ag substitution of Cu in concentrations as used in this study changed the dominating radiative recombination mechanism from BI transition: involving acceptor defects deeper than the mean energy depth of potential fluctuations in the CZTSSe monograins, to BT transition: involving localized acceptor-like states of the valence band tail in the ACZTSSe monograins.

3.2. Electrical characterization

3.2.1. Current-voltage measurement results

Following the successful substitution of Cu with Ag within the kesterite phase, a detailed investigation of its effect on the PV performance was performed. Current-voltage characterization of eight solar cells for each sample under AM1.5 illumination was carried out. The values of the open circuit voltage (V_{OC}), short circuit current (J_{SC}), fill factor (FF) and power conversion efficiency (η) of the solar cells are summarized in Fig. 6. The area of the solar cells is about 3.8 mm^2 and the presented η values are adjusted to the active area of the material. In fact, 75% of the actual area is covered with monograins where the rest of the area is polymer as shown in Additional Material Fig. A1b. For solar cells with × = 0.01, 0.02, and 0.03, the conversion efficiency consistently and reproducibly exceeded 8% and it is slightly higher than the reference devices. For those devices, the FF and the V_{OC} showed minor increase while the J_{SC} remained comparable to the reference cells. For devices containing the higher concentrations of Ag × = 0.04

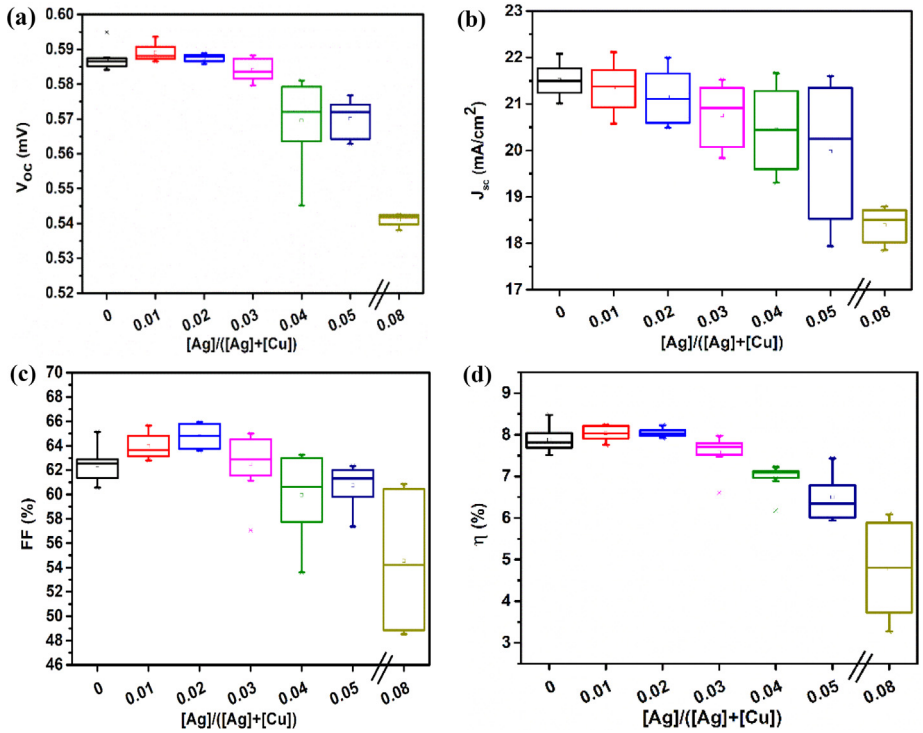

Fig. 6. Photovoltaic parameters of $(Ag_xCu_{1-x})_2ZnSn(S,Se)_4$ based monograin solar cells as a function of input Ag concentration measured under AM1.5 illumination, (a) open-circuit voltage (V_{OC}), (b) short circuit current (J_{SC}), (c) fill factor (FF) and (d) efficiency (η).

and 0.05, the overall conversion efficiency η was below 8% and the solar cells showed a tendency to lower performance with further increasing the Ag amount. In fact, the V_{OC} and the FF decreased causing the observed drop of efficiency while the J_{SC} remained comparable to the reference cells. The devices with × = 0.08 showed the lowest I-V parameters resulting in efficiencies below 6%.

3.2.2. The external quantum efficiency results

The external quantum efficiency (EQE) measurements were performed on the best solar cells of the eight series presented in Fig. 6. The measured EQE spectra of cells with × = 0, 0.02, 0.04 and 0.08 are exhibited in Fig. 7a. For all the investigated cells, the EQE spectra show equal losses up to 50% in the short wavelength region due to the absorption in the CdS buffer layer suggesting that the growth of the CdS layer was independent of the substitution of Cu by Ag. A maximum carrier collection was measured at a wavelength of around 540 nm, followed by steeply declining behaviour in the longer wavelength region where the photons are absorbed deeper in the absorber. The losses of the EQE at wavelengths higher than 540 nm increase with increasing the Ag amounts suggesting lower charge collection probability, which could be related to either weaker depletion field, and/or to the shorter charge carrier lifetimes presented in Fig. 2. The bandgaps (*Eg*) of the studied samples are estimated from the EQE spectra by plotting the $(EQE*E)^2$ against the photon energy (*E*). The interception of the linear part with the energy axis represents a reasonable estimation of the *Eg* as displayed in Fig. 7b (Oueslati et al., 2019). Analogously to previously reported results, we observed that a low level of Ag substitution of Cu (< 10%) has little influence on the bandgap of the absorber materials (Gershon et al., 2016) where the *Eg* shows only a slight blue-shift with higher Ag contents. Actually, the increase of the *Eg* with partial substitution of Cu by Ag is expected as the bandgap of CZTS and CZTSe is continuously tunable from 1.5 to 2.01 eV for CZTS and from 1.0 to 1.34 eV for CZTSe by substituting Cu by Ag (Li et al., 2018; Gong et al., 2015).

3.2.3. Impedance measurements results

The estimated capacitances evaluated from the impedance measurements at room temperature and at a fixed frequency of 100 KHz under DC voltage of 0 are presented in Fig. 8. Impedance Z and phase angle θ were both measured. An equivalent circuit, where a series resistance is followed by a resistance and a capacitance connected in parallel, was used for this evaluation. The impedance is consisting of a real and an imaginary part and it is described by the following equation (Kask et al., 2013):

$$Z = R_S + \frac{R_P}{1 + (\omega R_P C)^2} - i\frac{R_P{}^2 C\omega}{1 + (\omega R_P C)^2} \quad (6)$$

where ω, C, and R_P are angular frequency, capacitance, and parallel resistance, respectively. The estimated capacitance can be found by rewriting Eq. (6) as:

$$C = \frac{-Z''}{[(Z' - R_S)^2 + (-Z'')^2]\omega} \quad (7)$$

The estimated capacitance across the width of the space charge region (SCR) shows an increase from 1.9 nF for the Ag-free cell up to 3.2 nF for the cell with × = 0.08. The increase of capacitance values with increasing Ag amounts reveals an increase of the carrier concentration causing a reduction in the SCR width and affecting the carrier collection in the long wavelength region as shown in Fig. 7a.

3.2.4. Results of the temperature dependent current-voltage measurements

In order to gather more information about the electrical behaviour of the cells, temperature-dependent I-V measurements were performed under illumination. The behaviour of the V_{OC} of the cells as a function of the temperature $V_{OC}(T)$ is shown in Fig. 9a and can be described byw Eq. (8) (Kask et al., 2016):

$$V_{OC} = \frac{\Phi}{q} - \frac{Ak_BT}{q}\ln\left(\frac{J_{00}}{J_L}\right) \quad (8)$$

where Φ is the potential barrier for the dominant recombination path, *q*

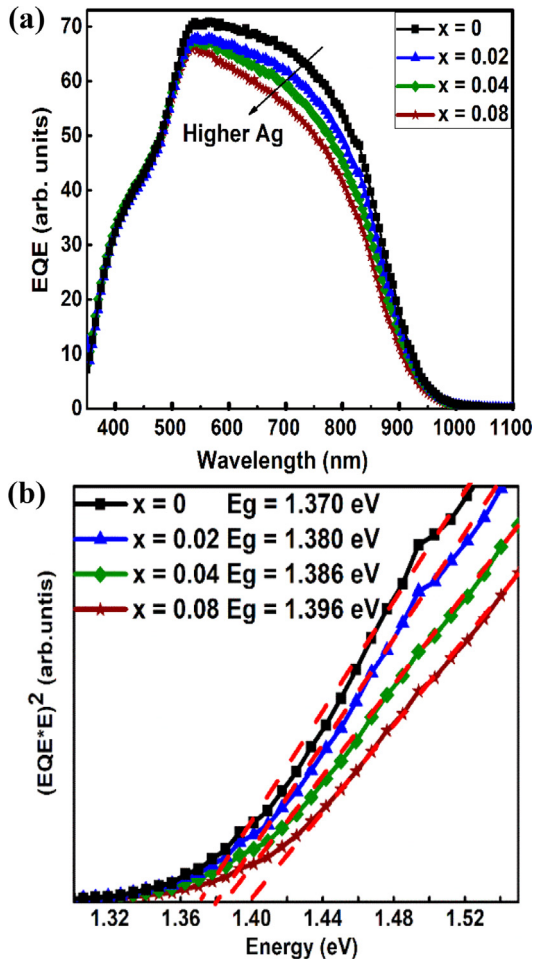

Fig. 7. EQE spectra for kesterite devices with different Ag contents (b) bandgap extraction by plotting $[(EQE*E)^2]$ vs. E.

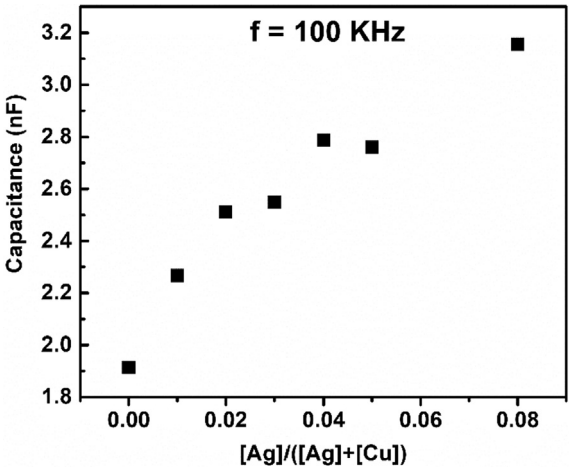

Fig. 8. Capacitance values at a fixed frequency of 100 KHz and a DC voltage of 0 for solar cell devices with different Ag contents.

is the elementary charge, A is the ideality factor, k_B is the Boltzmann constant, T is the temperature, J_{00} is the reverse saturation diode current prefactor and J_L is the light generated current density. At relatively high temperatures (above 200 K), the V_{OC} versus T shows linear behavior. The extrapolation of this linear part to T = 0 K indicates the potential barrier Φ. The activation energy values of the dominant recombination paths 1.22 eV, 1.20 eV, 1.18 eV, 1.20 eV and 1.12 eV for

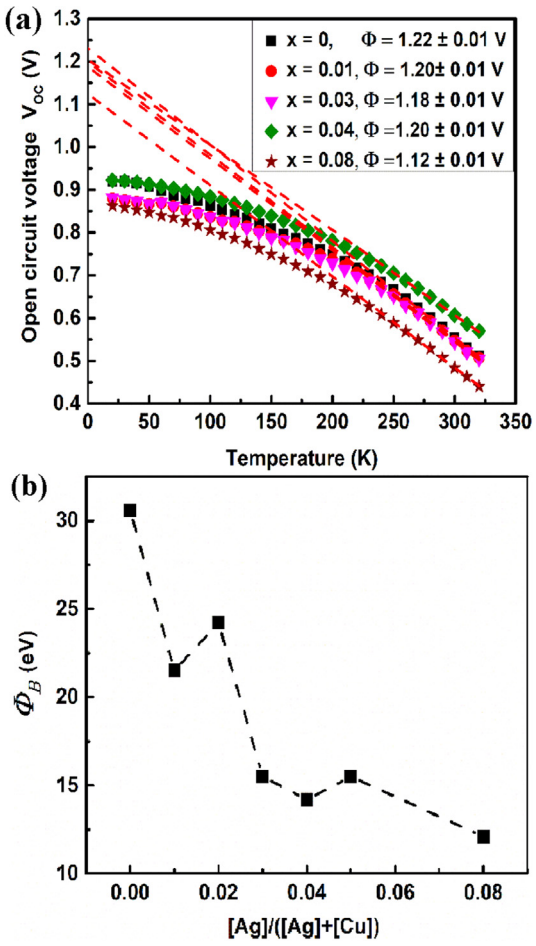

Fig. 9. (a) Open circuit voltage as a function of temperature (the straight lines are linear fits according to Eq. (8), (b) extracted activation energy from the series resistance R_S as a function of temperature for solar cells with different Ag contents.

devices with × = 0, 0.01, 0.03, 0.04 and 0.08, respectively, were found by dividing the Φ value by the elementary charge q. These activation energy values are significantly lower than the E_g values of ACZTSSe extracted from the EQE spectra suggesting that the dominant recombination channel in such solar cells is related to interface recombination, which inevitably causes large V_{OC} deficits (Oueslati et al., 2019; Brammertz et al., 2013).

The effect of the series resistance (R_S) of the devices at room temperature remains relatively small. However, the R_S increases exponentially as the temperature decreases as shown in Additional Material Fig. A5. The barrier height $\varnothing_B$ associated with the increase of R_S as a function of decreasing temperature can be estimated using Eq. (9) (Oueslati et al., 2015):

$$R_S = R_0 + B\exp\left(\frac{\varnothing_B}{kT}\right) \quad (9)$$

where B is a fitting parameter, $\varnothing_b$ is the barrier height and R_0 is the background R_S. R_0 is assumed to be weakly dependent on temperature and to dominate only at high temperatures (T ≥ 300 K). At lower temperatures, the exponential term will dominate and R_0 becomes negligible. An Arrhenius plot of the series resistance reveals that the energy of the activation barrier is decreasing monotonously with increasing Ag content as shown in Fig. 9b.

3.2.5. EBIC analysis result

For the electron beam induced current (EBIC) analysis, twin devices using the same investigated ACZTSSe monograins were prepared. The

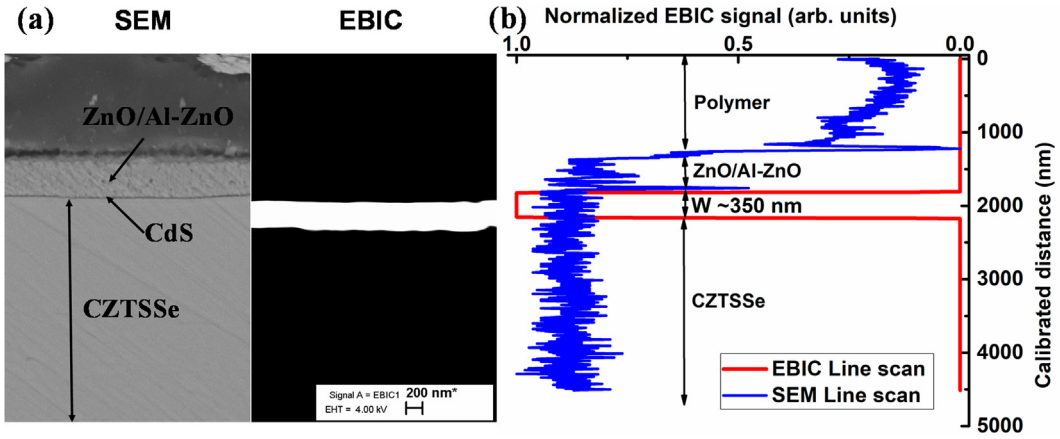

Fig. 10. (a) Simultaneously obtained secondary electron cross section image and photocurrent EBIC image (b) calibrated line scan of normalized EBIC signal and SEM micrograph.

images in Additional Material Fig. A6 are presented as a split picture showing on one side the secondary electron image and on the other side the photocurrent image obtained simultaneously from several monograins connected in a parallel configuration. The EBIC signal within the same monograin exhibits a continuous signal at the ACZTSSe/CdS interface showing a well-defined collection border following the grain's shape. It is worth to note that the discontinuity of the EBIC signal between different monograins exhibited in Additional Material Fig. A6 is due to the solar cell structure where the polymer is in between the working monograins. For better resolution and more accurate estimation of the EBIC signal width (W), higher magnification SEM & EBIC micrographs are shown in Fig. 10a, where the current amplification is increased in order to better identify the edges. Four devices with different amounts of Ag, x = 0, 0.02, 0.05 and 0.08, were investigated to study the variation of the EBIC signal width as a function of the Ag amount. An average of several EBIC profile lines extracted from the measured images of the investigated samples were used to extract the width W, as illustrated in Fig. 10b. The different layers of the solar cell structure are marked in the line scan picture. W was estimated to be about 350 nm for the Ag-free device. The EBIC line profiles obtained from the four investigated devices are depicted in Fig. 11. The change of the signal width W is clearly noticeable and it narrows with increasing Cu substitution by Ag. Thereby, the EBIC signal width decreases from 350 nm for the Ag-free device to 200 nm for the device with × = 0.08.

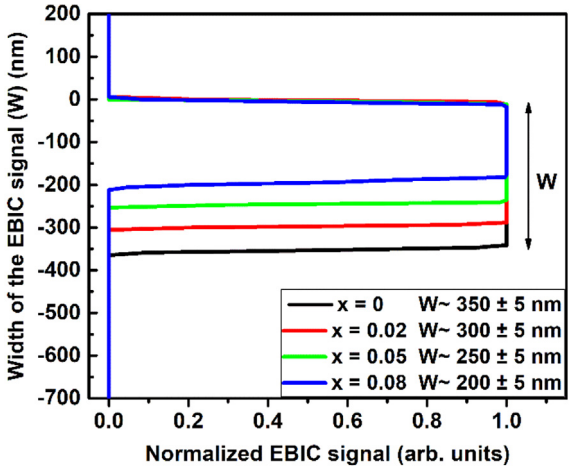

Fig. 11. Calibrated line scan of normalized EBIC signal as a function of devices with different Ag contents.

4. Discussion

The studied ACZTSSe samples were synthesized with relatively low Ag contents ($x \leq 0.08$) and seem to crystallize in tetragonal units with parameters close to those of the reference kesterite CZTSSe. The partial substitution of Cu by Ag in the CZTSSe monograins increases the degree of the cationic disorder and leads to higher defect concentrations. In fact, the elevated synthesis temperature of 740 °C needed to form ACZTSSe monograins provides the required thermal energy to randomize Cu, Ag and Zn in the unit cell, leading to a high density of antisite defects. Moreover, the added amounts of Cu were adjusted to a fixed ratio [Cu] + [Ag]/([Zn] + [Sn]) = 0.94 without taking into account that the added amounts of Ag were not totally incorporated in the kesterite structure as shown in Fig. 1a. Hence, Cu vacancies (V_{Cu}) seem to be the energetically favorable defects (Chen et al., 2013; Shin et al., 2017) and the concentration of V_{Cu} was predicted to increase significantly compared to the reference sample CZTSSe. The same assumption applies to CZTSSe absorbers when decreasing the Cu fraction from a Cu rich composition. This decrease in Cu-fraction leads to a material with higher p-type conductivity due to higher concentration of V_{Cu} defects (Vidani et al., 2018). According to the impedance measurements, the capacitance at a fixed frequency in the depletion region increased with increasing Ag content supporting the assumption that Cu/Ag deficit leads to higher doping concentrations. As a result, the ACZTSSe monograins had higher doping concentrations than the CZTSSe in contrast with other publications (Gershon et al., 2016; Guchhait et al., 2016; Qi et al., 2017).

The suggested change in the dominant recombination channel from BI transition for the CZTSSe sample to BT transition for ACZTSSe samples as studied by PL cannot solely be explained by the suppression of the acceptor level Cu_{Zn}. In fact, the change of the high valence band energy edge (connected with the Cu 3d-state and (S/Se) 3p-state antibonding) to a lower valence band edge (connected with hybridized states of the Cu 3d (Ag 4d) and (S/Se) 3p-state) could also contribute to the change of the nature of the radiative transition (Yuan et al., 2015). It is noted that the estimated barrier values $\varnothing_B$ extracted from R_S *(T)* decrease with increasing Ag amount, which could also be a consequence of the lower valence band energy edge after adding Ag or result from a change in the conduction band offset between CdS buffer layer and ACZTSSe absorber. The IV(T) study suggested that the dominant recombination channel in the whole solar cell device is at the CdS/CZTSSe heterojunction. Overall, the partial substitution of Cu by Ag in the CZTSSe solid solution leads to lower charge collection attributed to the higher carrier concentration after Ag incorporation or/and to the lower measured carrier lifetime. An increase of the carrier concentration tends to narrow the depletion width affecting the carrier

collection as also found in the EQE analysis. The length-scale of the variation of the EBIC signal W, as a function of the added Ag amounts, is in the order of hundred nanometers, indicating to the change of barrier height $\varnothing_B$ or/and to the change in the order of magnitude of doping. It was found that the efficiency for cells with $\times \leq 0.02$ was improved and higher Ag concentrations result in the decrease of the device efficiency nicely correlating with the trend of the measured carrier lifetime. The main contributing factors for the overall improvement or reduction of the efficiency are the V_{OC} and the FF. While the solar cells based on Ag-substituted CZTSSe absorbers showed higher bandgap compared to non-substituted absorbers, the changes in the V_{OC} are rather small and the V_{OC} deficit increases with increasing the Ag substitution.

5. Conclusions

Single phase $(Ag_xCu_{1-x})_2ZnSn(S,Se)_4$ monograins were synthesized in molten KI flux. The added Ag amounts were not totally incorporated into the kesterite structure leading to the Cu/Ag deficit in the synthesized materials, which increases the degree of cationic disorder and leads to higher defect concentrations. The thermal quenching of the photoluminescence emission can be well described by a single thermal activation energy, having lower values for the studied ACZTSSe monograins compared to the reference one. The Ag substitution of Cu by the amount used in this study changed the dominant radiative recombination mechanism from BI transition involving acceptor defects (deeper than the mean energy depth of fluctuations in the CZTSSe monograins) to BT transition involving localized acceptor-like states of the valence band tail in the ACZTSSe monograins. Higher carrier concentration and lower carrier lifetime were observed after Ag incorporation to CZTSSe leading to lower charge collection. The lower barrier height in the heterojunction and the higher doping concentrations after Ag incorporation in the kesterite material lead to lower collection width (smaller space charge region) as evaluated by the EBIC study. Partial substitution of Cu by Ag with small content ($x \leq 0.02$) increases slightly the FF and V_{OC} and leads to higher solar cells efficiencies, however higher Ag content does not have a positive impact on the solar cells parameters.

Declaration of Competing Interest

The authors declare that they have no known competing financial interests or personal relationships that could have appeared to influence the work reported in this paper.

Acknowledgements

This work was supported by institutional research funding IUT19-28 of the Estonian Ministry of Education and Research, by the Estonian Research Council grant PSG441 and by the European Union through the European Regional Development Fund, Projects TK141 and MOBJD308.

Appendix A. Supplementary material

Supplementary data to this article can be found online at https://doi.org/10.1016/j.solener.2020.02.002.

References

Barkhouse, D.A.R., Gunawan, O., Gokmen, T., Todorov, T.K., Mitzi, D.B., 2012. Device characteristics of a 10.1% hydrazine-processed $Cu_2ZnSn(Se, S)_4$ solar cell. Prog. Photovolt. Res. Appl. 20, 6–11. https://doi.org/10.1002/pip.1160.

Brammertz, G., Buffière, M., Oueslati, S., ElAnzeery, H., Ben Messaoud, K., Sahayaraj, S., Köble, C., Meuris, M., Poortmans, J., 2013. Characterization of defects in 9.7% efficient $Cu_2ZnSnSe_4$-CdS-ZnO solar cells. Appl. Phys. Lett. 103https://doi.org/10.1063/1.4826448. 163904.

Chen, S., Walsh, A., Gong, X.G., Wei, S.H., 2013. Classification of Lattice Defects in the Kesterite Cu_2ZnSnS_4 and $Cu_2ZnSnSe_4$ Earth-Abundant Solar Cell Absorbers. Adv. Mater. 25, 1522. https://doi.org/10.1002/adma.201203146.

Dale, P.J., Hoenes, K., Scragg, J., Siebentritt, S., 2009. A review of the challenges facing kesterite based thin film solar cells. In: Conf. Rec. IEEE Photovolt. Spec. Conf., Philadelphia, PA, 2080–2085. 10.1109/PVSC.2009.5411441.

Gershon, T., Lee, Y.S., Antunez, P., Mankad, R., Singh, S., Bishop, D., Gunawan, O., Hopstaken, M., Haight, R., 2016. Photovoltaic Materials and Devices Based on the Alloyed Kesterite Absorber $(Ag_xCu_{1-x})_2ZnSnSe_4$. Adv. Energy Mater. 6, 1502468. https://doi.org/10.1002/aenm.201502468.

Gershon, T., Sardashti, K., Gunawan, O., Mankad, R., Singh, S., Lee, Y.S., Ott, J.A., Kummel, A., Haight, R., 2016. Photovoltaic Device with over 5% Efficiency Based on an n-Type $Ag_2ZnSnSe_4$ Absorber. Adv. Energy Mater. 6, 1601182. https://doi.org/10.1002/aenm.201601182.

Gong, W., Tabata, T., Takei, K., Morihama, M., Maeda, T., Wada, T., 2015. Crystallographic and optical properties of (Cu, Ag)2ZnSnS4 and (Cu, $Ag)_2ZnSnSe_4$ solid solutions. Phys. Status Solidi C 12, 700–703. https://doi.org/10.1002/pssc.201400343.

Grossberg, M., Krustok, J., Timmo, K., Altosaar, M., 2009. Radiative recombination in $Cu_2ZnSnSe_4$ monograins studied by photoluminescence spectroscopy. Thin Solid Films 517, 2489–2492. https://doi.org/10.1016/j.tsf.2008.11.024.

Grossberg, M., Krustok, J., Raudoja, J., Timmo, K., Altosaar, M., Raadik, T., 2011. Photoluminescence and Raman study of $Cu_2ZnSn(Se_xS_{1-x})_4$ monograins for photovoltaic applications. Thin Solid Films 519, 7403–7406. https://doi.org/10.1016/j.tsf.2010.12.099.

Guchhait, A., Su, Z., Tay, Y.F., Shukla, S., Li, W., Leow, S.W., Tan, J.M.R., Lie, S., Gunawan, O., Wong, L.H., 2016. Enhancement of Open-Circuit Voltage of Solution-Processed Cu_2ZnSnS_4 Solar Cells with 7.2% Efficiency by Incorporation of Silver. ACS Energy Lett. 1, 1256–1261. https://doi.org/10.1021/acsenergylett.6b00509.

Hages, C.J., Redinger, A., Levcenko, S., Hempel, H., Koeper, M.J., Agrawal, R., Greiner, D., Kaufmann, C.A., Unold, T., 2017. Identifying the Real Minority Carrier Lifetime in Nonideal Semiconductors: A Case Study of Kesterite Materials. Adv. Energy Mater. 7, 1700167. https://doi.org/10.1002/aenm.201700167.

Jing, T., Dai, Y., Ma, X., Wei, W., Huang, B., 2015. Electronic Structure and Photocatalytic Water-Splitting Properties of $Ag_2ZnSn(S_{1-x}Se_x)_4$. J. Phys. Chem. C 119, 27900. https://doi.org/10.1021/acs.jpcc.5b09522.

Kanevce, A., Levi, D.H., Kuciauskas, D., 2013. The role of drift, diffusion, and recombination in time-resolved photoluminescence of CdTe solar cells determined through numerical simulation. Prog. Photovolt: Res. Appl. 22, 1138–1146. https://doi.org/10.1002/pip.2369.

Kask, E., Grossberg, M., Josepson, R., Salu, P., Timmo, K., Krustok, J., 2013. Mater. Sci. Semicond. Proc. 16, 992–996. https://doi.org/10.1016/j.mssp.2013.02.009.

Kask, E., Krustok, J., Giraldo, S., Neuschitzer, M., López-Marino, S., Saucedo, E., 2016. Temperature dependent electrical characterization of thin film $Cu_2ZnSnSe_4$ solar cells. J. Phys. D: Appl. Phys. 49, 085101. https://iopscience.iop.org/article/10.1088/0022-3727/49/8/085101.

Kauk-Kuusik, M., Li, X., Pilvet, M., Timmo, K., Grossberg, M., Raadik, T., Danilson, M., Mikli, V., Altosaar, M., Krustok, J., Raudoja, J., 2018. Study of $Cu_2CdGeSe_4$ monograin powders synthesized by molten salt method for photovoltaic applications. Thin Solid Films 666, 15–19. https://doi.org/10.1016/j.tsf.2018.09.025.

Krustok, J., Collan, H., Yakushev, M., Hjelt, K., 1999. The role of spatial potential fluctuations in the shape of the PL bands of multinary semiconductor compounds. Phys. Scr. 79, 179.

Krustok, J., Raudoja, J., Yakushev, M., Pilkington, R.D., Collan, H., 1999. On the Shape of the Close-to-Band-Edge Photoluminescent Emission Spectrum in Compensated $CuGaSe_2$. Phys. Status Solidi (a) 173, 483–490. https://doi.org/10.1002/(SICI)1521-396X(199906)173:2<483::AID-PSSA483>3.0.CO;2-A.

Krustok, J., Raadik, T., Jaaniso, R., Kiisk, V., Sildos, I., Marandi, M., Komsa, H.-P., Li, B., Zhang, X., Gong, Y., Ajayan, P.M., 2016. Optical study of local strain related disordering in CVD-grown $MoSe_2$ monolayers. Appl. Phys. Lett. 109, 253106. https://doi.org/10.1063/1.4972782.

Levanyuk, A.P., Osipov, V.V., 1981. Edge luminescence of direct-gap semiconductors. Sov. Phys. Usp. 24, 187–215. https://doi.org/10.1070/PU1981v024n03ABEH004770.

Li, S., Lloyd, M.A., Hempel, H., Hages, C.J., Márquez, J.A., Unold, T., Eichberger, R., McCandless, B.E., Baxter, J.B., 2019. Relating Carrier Dynamics and Photovoltaic Device Performance of Single-Crystalline $Cu_2ZnSnSe_4$. Phys. Rev. Appl 11, 034005. https://doi.org/10.1103/PhysRevApplied. 11.034005.

Li, J., Wang, D., Li, X., Zeng, Y., Zhang, Y., 2018. Cation Substitution in Earth-Abundant Kesterite Photovoltaic Materials. Adv. Sci. 5, 1700744. https://doi.org/10.1002/advs.201870021.

Nateprov, A., Kravtsov, V.C., Gurieva, G., Schorr, S., 2013. Single crystal X-ray structure investigation of $Cu_2ZnSnSe_4$. Surf. Eng. Appl. Electron. 49, 423–426. https://doi.org/10.3103/S1068375513050098.

Neubauer, C., Samieipour, A., Oueslati, S., Ernits, K., Meissner, D., 2018. Spatially resolved opto-electrical performance investigations of $Cu_2ZnSnS_{3.2}Se_{0.8}$ photovoltaic devices. Energy Sci Eng. 6, 563–569. https://doi.org/10.1002/ese3.232.

Oueslati, S., Brammertz, G., Buffière, M., Köble, C., Oualid, T., Meuris, M., Poortmans, J., 2015. Photoluminescence study and observation of unusual optical transitions in $Cu_2ZnSnSe_4$/CdS/ZnO solar cells. Sol. Energy Mater. Sol. Cells 134, 340–345. https://doi.org/10.1016/j.solmat.2014.10.041.

Oueslati, S., Brammertz, G., Buffière, M., ElAnzeery, H., Mangin, D., ElDaif, O., Touayar, O., Köble, C., Meuris, M., Poortmans, J., 2015. Study of alternative back contacts for thin film $Cu_2ZnSnSe_4$-based solar cells. J. Phys. D: Appl. Phys. 48, 035103. https://iopscience.iop.org/article/10.1088/0022-3727/48/3/035103/meta.

Oueslati, S., Grossberg, M., Kauk-Kuusik, M., Mikli, V., Ernits, K., Meissner, D., Krustok,

J., 2019. Effect of germanium incorporation on the properties of kesterite $Cu_2ZnSn(S, Se_)4$ monograins. Thin Solid Films 669, 315–320. https://doi.org/10.1016/j.tsf.2018.11.020.

Qi, Y., Tian, Q., Meng, Y., Kou, D., Zhou, Z., Zhou, W., Wu, S., 2017. Elemental Precursor Solution Processed $(Cu_{1-x}Ag_x)_2ZnSn(S, Se_)4$ Photovoltaic Devices with over 10% Efficiency. ACS Appl. Mater. Interfaces 9, 21243–21250. https://doi.org/10.1021/acsami.7b03944.

Shin, D., Saparov, B., Mitzi, D.B., 2017. Defect Engineering in Multinary Earth-Abundant Chalcogenide Photovoltaic Materials. Adv. Energy Mater. 7, 1602366. https://doi.org/10.1002/aenm.201602366.

Shockley, W., Queisser, H.J., 1961. Detailed balance limit of efficiency of p-n junction solar cells. J. Appl. Phys. 32, 510. https://doi.org/10.1063/1.1736034.

Siebentritt, S., 2013. Why are kesterite solar cells not 20% efficient? Thin Solid Films 535, 1–4. https://doi.org/10.1016/j.tsf.2012.12.089.

Sulimov, M.A., Yakushev, M.V., Forbes, I., Prieto, J.M., Mudryi, A.V., Krustok, J., Edwards, P.R., Martin, R.W., 2019. A PL and PLE Study of High Cu Content $Cu_2ZnSnSe_4$ Films on Mo/Glass and Solar Cells. Phys. Solid State 61, 908–917. https://doi.org/10.1134/S1063783419050214.

Vidani, A.C., Haass, S.G., Andres, C., Caballero, R., Figi, R., Schreiner, C., Márquez, J.A., Hages, C., Unold, T., Bleiner, D., Tiwari, A.N., Romanyuk, Y.E., 2018. High-Efficiency $(Li_xCu_{1-x})_2ZnSn(S, Se_)4$ Kesterite Solar Cells with Lithium Alloying. Adv. Energy Mater. 8, 1801191. https://doi.org/10.1002/aenm.201801191.

Wang, W., Winkler, M.T., Gunawan, O., Gokmen, T., Todorov, T.K., Zhu, Y., Mitzi, D.B., 2014. Device Characteristics of CZTSSe Thin-Film Solar Cells with 12.6% Efficiency. Adv. Energy Mater. 4. https://doi.org/10.1002/aenm.201301465.

Yakusheva, M.V., Sulimov, M.A., Márquez-Prieto, J., Forbes, I., Krustok, J., Edwards, P.R., Zhivulko, V.D., Borodavchenko, O.M., Mudryi, A.V., Martin, R.W., 2017. Influence of the copper content on the optical properties of CZTSe thin films. Sol. Energy Mater. Sol. Cells 168, 69–77. https://doi.org/10.1016/j.solmat.2017.04.022.

Yuan, Z., Chen, S., Xiang, H., Gong, X., Walsh, A., Park, J., Repins, I., Wei, S., 2015. Engineering Solar Cell Absorbers by Exploring the Band Alignment and Defect Disparity: The Case of Cu- and Ag-Based Kesterite Compounds. Adv. Funct. Mater. 25, 6733–6743. https://doi.org/10.1002/adfm.201502272.